LAWRENCE
LIVERMORE
NATIONAL
LABORATORY

UCRL-JRNL-220815

Predicting dissolution patterns in variable aperture fractures: 1. Development and evaluation of an enhanced depth-averaged computational model

R. L. Detwiler, H. Rajaram

April 24, 2006

Water Resources Research

Updated October 14, 2003

Predicting dissolution patterns in variable aperture fractures: 1. Development and evaluation of an enhanced depth-averaged computational model

Russell Detwiler
Lawrence Livermore National Laboratory, University of California, Livermore, California, detwiler@llnl.gov
Harihar Rajaram
Department of Civil, Environmental and Architectural Engineering, University of Colorado, Boulder, Colorado

Abstract

Water-rock interactions within variable-aperture fractures can lead to dissolution of fracture surfaces and local alteration of fracture apertures, potentially transforming the transport properties of the fracture over time. Because fractures often provide dominant pathways for subsurface flow and transport, developing models that effectively quantify the role of dissolution on changing transport properties over a range of scales is critical to understanding potential impacts of natural and anthropogenic processes. Dissolution of fracture surfaces is controlled by surface-reaction kinetics and transport of reactants and products to and from the fracture surfaces. We present development and evaluation of a depth-averaged model of fracture flow and reactive transport that explicitly calculates local dissolution-induced alterations in fracture apertures. The model incorporates an effective mass transfer relationship that implicitly represents the transition from reaction-limited dissolution to transport-limited dissolution. We evaluate the model through direct comparison to previously reported physical experiments in transparent analog fractures fabricated by mating an inert, transparent rough surface with a smooth single crystal of potassium dihydrogen phosphate (KDP), which allowed direct measurement of fracture aperture during dissolution experiments using well-established light transmission techniques [*Detwiler, et al*., 2003]. Comparison of experiments and simulations at different flow rates demonstrate the relative impact of the dimensionless Peclet and Damkohler numbers on fracture dissolution and the ability of the computational model to simulate dissolution. Despite some discrepancies in the small-scale details of dissolution patterns, the simulations predict the evolution of large-scale features quite well for the different experimental conditions. This suggests that our depth-averaged approach to simulating fracture dissolution provides a useful approach for extending laboratory results that are often limited in scale to scales that are more representative of geologic processes of interest.

1.0 Introduction

Reactive fluid flow in fractured media can cause dissolution of minerals along fracture surfaces leading to localized changes in fracture apertures. Local dissolution rates are controlled by the advective and diffusive transport of reactants and products within the fracture and the kinetics of chemical reactions occurring at the rock-water interfaces. In unfractured porous limestone cores, the relative rates of these processes, which are often quantified by the dimensionless Peclet number (*Pe* a measure of the relative strength of advection/diffusion) and Damkohler number (*Da*, a measure of the relative strength of reaction/advection), both of which are defined for single fractures in Section 2, have been shown to result in a wide range of dissolution patterns [e.g., *Hoefner and Fogler*, 1988; *Daccord, et al.*, 1993]. For advection-limited systems (low Pe and high Da), reaction kinetics and/or molecular diffusion are rapid enough that reactants are consumed within a short distance of the entrance, resulting in uniform dissolution of the rock face. At the other extreme very slow reaction rates (low Da) result in nearly uniform dissolution throughout the core. Between these two extremes, regions with higher permeability experience greater local flow rates, leading to more rapid mass transfer between the flowing fluid and the mineral surfaces within the pore volume. This nonlinear, positive feedback results in a rich variety of behaviors from compact dissolution channels (wormholes) to highly ramified structures. Because fractures provide dominant pathways for flow and transport, developing a quantitative understanding of the long-term evolution of transport properties during reactive fluid flow over a range of scales is critical to understanding processes such as the formation of karst systems, acid injection for stimulating petroleum wells, and injection and leakage rates in subsurface CO_2 storage schemes.

Despite numerous investigations of dissolution in cores of consolidated porous media [see *Golfier, et al.*, 2002 for a recent overview], relatively few studies have focused on the dissolution of fracture surfaces. This is largely due to the difficulty of detailed experimentation, particularly quantifying the influence of the initial spatially variable fracture aperture field, on the outcome of a given experiment. In porous media, it is

relatively straightforward to create or obtain cores with homogeneous porosity and permeability distributions over many representative elementary volumes (REVs), but creating or finding fractures with similar initial geometries, or even defining the REV, is challenging. Thus, recent efforts to understand the role of dissolution on fractures have focused on quantifying the aperture fields before and after dissolution experiments using either surface profilometry to measure fracture surfaces [*Durham, et al.*, 2001] or direct measurement of fracture apertures using energy transmission techniques such as high-resolution x-ray computed tomography (CT) [*Gouze, et al.*, 2003], nuclear magnetic resonance imaging (NMR) [*Dijk, et al.*, 2002], and light transmission through transparent analog fractures [*Detwiler, et al.*, 2003].

Experimental investigations of fracture dissolution to date have shown a range of behaviors due to differences in experimental conditions, which poses challenges for interpreting the relative influence of parameters such as Pe, Da and aperture variability on the observed behavior. Surface profilometry measurements of a 4.7 x 7.2-cm fractured calcite core with the surfaces placed in contact under a 0.2 MPa confining stress [*Durham, et al.*, 2001] showed a reduction in small-scale aperture variability and the formation of a broad channel in the reconstructed aperture field. *Gouze et al.* [2003] used high-resolution x-ray CT (~5 μm voxels) to measure changes in the surface topography and aperture in two small (0.6 x 1.2 cm) fractured cores. One core was pure calcite, similar to that used by *Durham et al.* [2001] and the other contained ~15% secondary minerals. The pure calcite core exhibited uniform dissolution over the fracture surfaces, which at the scale of the experiment, is similar to the results observed by *Durham et al.* [2001]. However, the presence of secondary minerals in the second experiment led to preferential dissolution of the calcite grains and significant roughening of the fracture surfaces. In 1.8 x 3.6-cm fractured halite cores with the surfaces propped apart with an initial separation of ~2 mm, *Dijk et al.* [2002] used NMR imaging to directly measure fluid velocities and apertures and showed a rough correlation between changes in aperture and local fluid velocities with differences between samples attributed to varying degrees of impurities in the samples and buoyancy effects. *Detwiler et al.* [2003] removed the influence of mineral heterogeneity by fabricating 9.9 x 15.2-cm transparent

analog fractures consisting of a smooth, homogeneous potassium-dihydrogen-phosphate (KDP) crystal mated with rough glass. High-resolution light transmission measurements of the evolving aperture field at two different initial flow rates demonstrated the formation of distinct dissolution channels at low Pe (high Da), and more uniform growth of the fracture aperture at high Pe (low Da). Due to the wide range of results for experiments under different conditions, and the limited number of experiments reported in each of these studies, uncertainty remains regarding the relative influence of the underlying reaction and transport mechanisms on fracture dissolution. Furthermore, the one common feature of all of the cited studies is the limited size of the experiments, which presents challenges in predicting how the small-scale processes will manifest at the scale of geologic processes of interest.

Development of efficient computational models provides a potential path towards enhanced understanding of the role of local reaction and transport processes on fracture dissolution over a wider range of parameters and scales than is possible in the laboratory. For this approach to be effective, models must adequately represent the three-dimensional velocity field within the fracture and the resulting transport of dissolved minerals, including boundary conditions representing the relevant surface reactions. Models have been developed that directly solve finite-difference approximations to the three-dimensional Stokes equations and advection-diffusion-reaction equation [*Bekri, et al*., 1997] or use particle tracking in a three-dimensional velocity field calculated using lattice-Boltzmann (LB) techniques [*Verberg and Ladd*, 2002; *Szymczak and Ladd*, 2004]. Recent efforts to test these computational models of fracture dissolution with quantitative experimental results have met with mixed results. *Verberg and Ladd* [2002] simulated the experiment of *Durham et al*. [2001] and demonstrated that the model predicted smoothing of small-scale aperture variability and increased large-scale channeling (as observed in the experiment), but the extent and location of the large scale channels were in poor agreement with the experimental results. They attributed the discrepancies to crude models of reaction kinetics and fracture closure. *Szymczak and Ladd* [2004] demonstrated an enhanced LB dissolution model with improved representation of reaction kinetics at the fracture surfaces [*Szymczak and Ladd*, 2003] by comparing

simulations to the experiments of *Detwiler et al.* [2003]. To use their model to simulate the dissolution of the KDP surface, they used a linear approximation to represent the nonlinear reaction kinetics of KDP and broke the 9.9 x 15.2 cm domain into three equal pieces to circumvent memory constraints of the LB algorithm. Their simulations demonstrated excellent qualitative agreement with the simulations and experiments. This suggests that if velocity variations within a fracture are adequately represented and the surface reaction kinetics are effectively quantified, fracture dissolution patterns can be reproduced quite well. However, due to the small length scales associated with velocity variations across the fracture aperture ($O(10^{-5})$ m) and in the fracture plane ($O(10^{-4})$ m), direct solution of the three-dimensional equations is computationally costly, limiting the scales at which these processes can be simulated.

An alternative approach for modeling dissolution in variable aperture fractures is to integrate the three-dimensional governing equations between the fracture surfaces and incorporate a depth-averaged mass-transfer relationship for calculating local reaction rates. This approach was originally presented by *Hanna and Rajaram* [1998] where they demonstrated the influence of the magnitude of aperture variability on the rate of dissolution channel formation in karst systems, and more recently, *O'Brien et al.* [2003] simulated dissolution of a fracture in quartzite due to hydrothermal fluid flow. However, the assumptions required for development of the depth-averaged models have not been evaluated through rigorous comparison to experimental results. In particular, these models require development of an effective mass-transfer relationship in terms of local depth-averaged concentrations. O'Brien et al. [2003] simply used a linear kinetic reaction rate to quantify quartzite dissolution thereby assuming that mass transfer was reaction-rate limited. To allow for the possibility of transport-limited reactions, *Hanna and Rajaram* [1998] assumed that surface reactions and transport of dissolved minerals from the fracture surface occur in series and thus the slower process will control the local reaction rate. They used a mass transfer relationship for flow between parallel plates to quantify transport-limited reaction rates.

In this paper, we develop an enhanced depth-averaged fracture dissolution model and directly compare the model to the quantitative experimental results of *Detwiler et al.* [2003]. The enhanced model incorporates a modified expression for the local reaction rate coefficient that implicitly represents the transition from transport-limited reactions to rate-limited reactions. In addition, to minimize resolution-dependent errors caused by numerical dispersion, we have incorporated a bounded higher-order upwinding scheme [*Alves, et al.*, 2003] for discretizing the advective term in the transport equation. Direct comparisons to experimental results demonstrate that this enhanced model predicts experimental measurements of the influence of Pe and Da on the dissolution of a variable aperture fracture. Furthermore, the simulation results are demonstrated to be independent of grid-resolution as long as the initial aperture variability is adequately represented. The remainder of the paper is structured as follows: Section 2 presents an overview of the computational model development; Section 3 describes the experimental setup and summarizes the experimental results; Section 4 compares results of simulations in the measured aperture fields to the experimental measurements and explores the sensitivity of the model to grid resolution; and Section 5 includes a discussion of the results and concluding remarks.

2.0 Computational Model

Conservation equations integrated between the fracture surfaces are used to calculate the depth-averaged pressures, concentrations and local reaction rates, which lead to corresponding alterations of local fracture apertures. Efforts to evaluate depth-averaged flow equations through comparison to experiments [e.g., *Yeo, et al.*, 1998; *Nicholl, et al.*, 1999] and three-dimensional solutions to the Navier-Stokes equations [e.g., *Mourzenko, et al.*, 1995; *Brush and Thomson*, 2003] have demonstrated that effective transmissivity is typically overestimated. However, for fractures with aperture statistics representative of many natural fractures ($\sigma_b/\langle b\rangle<1$ and $\langle b\rangle/\lambda<0.5$) the discrepancies between the depth-averaged flow equation and the three-dimensional Navier-Stokes equations are less than 10% [e.g., *Brush and Thomson*, 2003], which supports developing a fracture dissolution

model based upon the depth-averaged flow equation. The depth-averaged approach is further reinforced by simulations of the dissolution of entrapped nonaqueous-phase-liquids [*Detwiler, et al.*, 2001] using velocity fields derived from the depth-averaged pressure fields that demonstrated excellent agreement with experiments when the flow rate through the fracture is prescribed to match experimental flow rates. This suggests that, despite the simplifying assumptions required in developing the depth-averaged models, they may provide a useful tool for simulating the influence of surface reactions on alterations in fracture aperture and transmissivity.

The depth-averaged approximation to the three-dimensional Stokes equations for flow through a fracture is:

$$\frac{\partial b}{\partial t} + \nabla \cdot \mathbf{q} = 0 \tag{1}$$

where b is the local aperture, the local flux $\mathbf{q}$ is given by:

$$\mathbf{q} = -\frac{b^3 g}{12\nu} \nabla h \tag{2}$$

and h is the local hydraulic head. Transport of a dissolved mineral is represented using a depth-averaged reactive transport equation:

$$\frac{\partial (bc)}{\partial t} + \nabla \cdot (\mathbf{q}c) - \nabla \cdot (b\mathbf{D}\nabla c) = R(c) \tag{3}$$

where c is the depth-averaged concentration of the dissolved mineral, $R(c)$ represents the local effective reaction rate, and $\mathbf{D}$ is a local dispersion tensor that can account for both molecular diffusion and Taylor dispersion, which arises due to velocity gradients across the fracture aperture [e.g., *Detwiler, et al.*, 2000]. Note that this representation of $\mathbf{D}$ assumes that the model adequately represents velocity variations in the fracture plane

such that macrodispersion occurs implicitly without the need for a macrodispersion tensor. Furthermore, sensitivity studies for simulations of the dissolution of nonaqueous-phase liquids from a variable aperture fracture [*Detwiler, et al.*, 2001] and dissolution of fracture walls [*Cheung*, 2002] have demonstrated that a local velocity-dependent dispersion tensor has a negligible influence on mass transfer rates, thus for the current study, we set **D** equal to the molecular diffusion coefficient (D_m).

Local reactions lead to alterations of the fracture aperture:

$$\frac{\partial b}{\partial t} = \frac{R(c)}{\alpha \rho_r} \tag{4}$$

where ρ_r is the density of the dissolving mineral and α is a stoichiometric coefficient that represents the mass of mineral entering solution for a unit mass of dissolved rock. For the idealized case of very slow reaction rates and first-order reaction kinetics, we can approximate local reaction rates using:

$$R(c) = k(c_s - c) \tag{5}$$

where k (m/s) is the surface reaction rate coefficient and c_s is the equilibrium concentration of the dissolving mineral.

When the dimensionless parameter $\varepsilon = (c_s - c_o)/\rho_r << 1$, where c_o is the influent concentration of the dissolving mineral, the time scale required for the pressure and concentration fields to reach equilibrium is much shorter than the time scale required for significant alteration of the fracture apertures [see *Hanna and Rajaram*, 1998 for details] allowing the use of quasi-steady approximations of the pressure and concentration fields. Thus, during each time step, the steady-state approximations of (1) and (3) provide the pressure and concentration distributions within the fracture and local reaction rates, which are then used to incrementally alter fracture apertures.

Nondimensionalizing the quasi-steady approximations to (3) results in:

$$\nabla \cdot \left(\mathbf{q}' c'\right) - \frac{1}{Pe}\frac{\langle b \rangle}{L}\nabla \cdot b' \nabla c' = Da\left(1 - c'\right)$$

$$b' = \frac{b}{\langle b \rangle} \qquad x' = \frac{x}{L} \qquad y' = \frac{y}{L} \qquad c' = \frac{c}{c_s} \qquad \mathbf{q}' = \frac{\mathbf{q}}{\langle \mathbf{q} \rangle} \tag{6}$$

$$Pe = \frac{\langle \mathbf{q} \rangle}{D_m} \qquad Da = \frac{kL}{\langle \mathbf{q} \rangle}$$

where $\langle\rangle$ represents an average over the domain and L represents the fracture length. *Pe* quantifies the relative magnitude of advection to diffusion over length scales on the order of $\langle b \rangle$, the implicit length scale associated with $\langle q \rangle$. This definition of *Pe* is consistent with most previous investigations of transport processes in single fractures. For $Pe<1$, diffusion will dominate and dampen any perturbations in the evolving reaction front, whereas for $Pe>1$, advection will dominate and allow perturbations along the reaction front to persist. Consequently, the tendency of small perturbations in the reaction front to grow into distinct dissolution channels is controlled by *Da*, which is defined at the fracture scale (*L*). For $Da<<1$, reaction rates will be sufficiently slow that undersaturated fluid will traverse the length of the fracture, with local mass transfer rates controlled by surface reaction rates, suppressing the growth of reaction-front instabilities. At larger values of *Da*, surface reactions are rapid and the fluid will become saturated within the length of the fracture, resulting in the development of distinct dissolution channels within the fracture.

Development of (6) presumes slow surface reaction kinetics; however, as reaction rates increase, the transport of dissolving minerals from the surface can limit reaction rates. For infinitely fast surface reactions, local reaction rates are controlled solely by transport

of dissolving minerals and can be quantified by an effective mass transfer relationship of the form:

$$R(c) = \frac{ShD_m}{b}(c_s - c) \tag{7}$$

where, *Sh* is the dimensionless Sherwood number. For mass transfer between parallel plates where the dissolved concentrations are at equilibrium at the reacting surfaces, the asymptotic value of Sh is 3.78 [*Kays*, 1966]. The entry length required to reach the asymptotic value is approximately $0.1bPe$ [e.g., *Rohsenow and Choi*, 1961] suggesting that a constant value of *Sh* is appropriate beyond a relatively short entry length.

By assuming that surface reactions and mass transport of reactants occur in series, *Hanna and Rajaram* [1998] used the lesser of (5) and (7) to calculate local dissolution rates. In this study, we develop a local mass transfer relationship that effectively accounts for both hydrodynamics and surface reaction kinetics through the use of a single effective reaction rate coefficient. Equations (5) and (7) suggest that a modified local Damkohler number of the form:

$$Da' = \frac{kb}{ShD_m} \tag{8}$$

provides a measure of the relative influence of surface reaction kinetics to mass transport on the local mass transfer rates. That is, local reaction rates are controlled by surface reactions for $Da' >> 1$ and transport of dissolving minerals from the fracture surfaces for $Da' << 1$. Note that our definition of Da' is analogous to dimensionless parameters used in previous studies including the kinetic number (K_i) [e.g., *Daccord, et al*., 1993; *Golfier, et al*., 2002] and *PeDa* as defined by *Bekri et al*. [1997]. To effectively model this range of behaviors, including the transition that occurs near $Da' = 1$, we define an effective reaction rate coefficient:

$$k_{eff} = \frac{k}{1 + Da'} \tag{9}$$

which is similar in form to an expression for the effective reaction rate for transient reactive transport through a circular tube [*Johns and Degance*, 1975]. This expression for k_{eff} reduces to k in the limit of small Da' and approaches ShD_m/b for large Da'. Thus, using k_{eff} to replace k in (5) provides a single expression for effectively representing the depth-averaged mass-transfer rate over the range of Da' (**Figure 1**). At small values of Da', $R(c)$ is bounded by the surface reaction kinetics and at large values of Da', $R(c)$ asymptotically approaches the effective mass transfer relationship given by (7). In the region around $Da'=1$, k_{eff} provides a smooth transition between the two limiting behaviors. In the Appendix, we demonstrate that (9) accurately matches results from mass transfer simulations between parallel plates and theoretical expressions for the mass transfer coefficient derived by *Walker and Davies* [1974].

To numerically calculate reactive fluid flow and the resulting dissolution-induced changes in fracture aperture, we discretize the governing equations on a uniform grid using finite difference approximations. For the flow equation, we use a centered-finite-difference discretization of (1) and solve the resulting system of equations with an efficient algebraic multigrid (AMG) solver [e.g., *Ruge*, 1988; *Detwiler, et al.*, 2002]. We discretize the transport equation (3) using centered differences for the diffusive term and a bounded higher order upwinding scheme for the advective term [*Alves, et al.*, 2003]. For the case of nonlinear reaction kinetics, Newton-Raphson iteration provides efficient solution of the nonlinear transport equation. The reactive surface area within each grid block is taken to be the projected area of the grid block (i.e. $\Delta x \cdot \Delta y$), which for our experimental system is a reasonable assumption. However, we note that for some rock surfaces this may result in a significant underestimation of the reactive surface area [e.g., *Gouze, et al.*, 2003].

3.0 Overview of experiments

To test the computational model, we carried out a set of fracture dissolution experiments. Preliminary details of these experiments were reported by *Detwiler et al.* [2003]. Here we provide a brief overview of the experimental procedures and include additional details that are particularly relevant to quantitative comparison with numerical simulations.

We fabricated 9.9 x 15.2-cm transparent analog fractures by mating flat KDP surfaces with a rough glass surface. The surfaces were initially placed in contact and then held at constant displacement by a rigid aluminum test frame. This procedure results in transparent analog fractures with initial aperture fields that can be replicated from one experiment to the next by mating the same rough glass surface with a new KDP crystal. Furthermore, the uniform, well-characterized surface-reaction kinetics at the KDP-water interface provide the unique opportunity to separate the influence of aperture variability from surface-mineral heterogeneity on the dissolution process. We present the results from two experiments in which we imposed different hydraulic gradients across the fracture leading to different values of *Pe* and *Da* for each experiment (see **Table 1** for a summary of experimental conditions). Note that the statistics of the initial fracture aperture field are representative of reported values for measured apertures in natural fractures [e.g. *Brown*, 1995; *Detwiler, et al.*, 1999].

During each experiment, light transmission measurements and the Beer-Lambert law of light absorption provided measurements of the changes in fracture aperture caused by flow of the undersaturated KDP solution through the variable-aperture fractures [*Detwiler, et al.*, 2003]. Warner Jenkins FD&C Blue #1 dye (0.0125 g/l) added to the influent solution enhanced differential light absorption throughout the fracture and a 12-bit charge-coupled device (CCD) camera provided accurate, high-resolution (83 x 83 μm pixels) measurements of light transmitted through the fracture. A narrow band-pass filter on the camera reduced the width of the spectrum of the measured light to a narrow range centered on the absorbance spectrum peak for the dye to enhance measurement accuracy. Direct measurement of fracture apertures requires sequentially filling an unchanging

fracture aperture with clear and dyed solutions [*Detwiler, et al.*, 1999]. Because this was not possible during our dissolution experiments, we used a modified application of the Beer-Lambert law of light absorption [see *Detwiler, et al.*, 2003] to directly measure changes in fracture aperture during experiments. These measurements were subsequently combined with an independent measurement of the initial fracture aperture field obtained by mating the rough glass surface with a 12 mm-thick, optically flat sample of fused quartz. Light transmission techniques [*Detwiler, et al.*, 1999] then provided accurate (±2 μm) full-field measurements of the initial fracture aperture field (**Figure 2**).

Aligning the measured Δb fields from each experiment with the measurement of the initial aperture field was an image processing challenge that arose during analysis of the experimental results. Despite careful efforts to align each fracture during assembly and attachment to the test stand, some misalignment was inevitable. We realigned the images by defining registration marks on each image and applying a perspective transformation [*Jähne*, 1997] to align the initial aperture field with the experimental images. Bilinear interpolation provided the aperture values on the transformed coordinate system. This registration procedure results in larger errors in local apertures measured during experiments, but based on our previous analyses of measurement errors [*Detwiler, et al.*, 1999], we estimate accuracies of about ±4 μm for apertures measured during the dissolution experiments.

4.0 Comparison of simulations with experiments

The aperture fields measured during the experiments provide the basis for a detailed evaluation of the computational model presented in Section 2.0. This requires replacing (5) with an expression representing the reaction kinetics of KDP. A birth-and-spread dissolution model can be used to represent the surface reaction kinetics:

$$R(c') = A(1-c')^{5/6} \exp\left[-B/(1-c')\right] \tag{10}$$

where A and B are parameters that have been empirically quantified for different facets of KDP crystals [*Koziejowska and Sangwal*, 1988]. For implementation in (5), we did not use (10) directly, but replaced it with a modified form of (5) with a reaction rate coefficient that is dependent on the local concentration. Replacing the exponent of 5/6 with 1 and A and B with modified parameters A′ and B′ (see **Table 2**) leads to a simplified expression (11) for the surface reaction rate coefficient in (5) with a negligible discrepancy from (10) (**Figure 3**):

$$k(c') = \frac{A' \exp\left[-B' / (1 - c')\right]}{c_s} \tag{11}$$

It is also necessary to modify *Sh* in (8) to account for the fact that only one fracture surface is dissolving in our experimental system. For a parallel plate system with one surface at equilibrium and the other a no-flux boundary, the appropriate asymptotic value of Sh is 2.43 [*Kays*, 1966]. Also note that inclusion of $k(c')$ in (11) into (8) results in concentration dependent expression for k_{eff} and a nonlinear advection-diffusion-reaction equation.

To evaluate the depth-averaged mass transfer model, we simulated flow of the experimental fluid through the measured initial aperture fields and directly compared the simulations to the experimentally measured aperture fields acquired during each of the experiments. **Table 2** summarizes the parameters and boundary conditions used for these simulations and highlights the fact that each of the parameters have been obtained from independent measurements or sources, not through model calibration. The constant hydraulic gradients for the two simulations were specified such that the initial flow rates matched the measured experimental flow rates. **Figure 4** shows cumulative outflow mass from the experiments and simulations. The results demonstrate good agreement between both the initial flow rates and the change in flow rates as the fracture aperture increased. Discontinuities in the measured cumulative outflow mass for Exp. 1 resulted from the removal of KDP that had precipitated at the constant head outlet port. The gradual

precipitation of KDP led to gradual increases in hydraulic gradient, and after removal (~4 and 12.5 hours), the gradient was restored to the initial value. However, despite these small fluctuations in experimental flow rates, after the corrections to the experimental gradient, the flow rates for the experiment and simulations are in good agreement.

The evolution of the fracture aperture fields for the two experiments and the corresponding simulations can be directly compared. **Plates 1a and 1b** show Δb fields for Exp. 1 and 2 with the corresponding simulations at $\langle b \rangle / \langle b_o \rangle$ = 1.3, 1.7, and 2.1. For Exp. 1 (**Plate 1a**), narrow channels observed at early time compete for flow as the channels evolve. At later times, two dominant channels become evident, with one eventually reaching the outflow boundary first, at which time it begins to grow faster at the expense of the other channels. By contrast, for Exp. 2 (**Plate 1b**), the narrow channels at early time are less distinct resulting in a more uniform growth of the fracture aperture. The most significant difference between the simulations and experiments is that, in the regions nearest the tips of the growing channels, the simulations predict smoother growth of the apertures, whereas the experiments exhibit more variability in local dissolution rates. Closer inspection of a growing channel tip clarifies the nature of the discrepancies in these small-scale details (**Plate 1c**). In the experiment, the channels are more focused, with the local regions of greatest growth corresponding with regions of smaller apertures, whereas the simulation yields more diffuse channels and a weaker inverse correlation with aperture. These small-scale discrepancies are likely due to inherent limitations with the depth-averaged models of flow and transport of the dissolving KDP and mass transfer using k_{eff}. However, despite the differences between the simulations at scales of the order of λ, the large-scale features of both experiments are predicted quite well by the simulations. The most significant large-scale discrepancy between the experiments and simulations occurred for Exp. 2, where red and green near the inflow boundary in the experimental field at $\langle b \rangle / \langle b_o \rangle$=2.0 indicate more dissolution than was predicted by the corresponding simulation. This may be due to our use of the asymptotic value of Sh in the entry region (x<~0.1$Pe\langle b \rangle$), which is less than 3 mm at early time, but increases during the experiment as both Pe and $\langle b \rangle$ increase in the inflow region. However, beyond the relatively short entry region, agreement between the experiment and simulation is good.

Because our primary interest is in developing a model that may be used to explore scaling properties of fracture dissolution, we consider several fracture-scale measures of the ability of the simulations to predict the dissolution-induced changes in fracture properties. Plotting relative changes in mean aperture against time (**Figure 5**) demonstrates that the rate of mean aperture growth is predicted quite well for both experiments. This suggests that the model is quite accurate in representing the fracture-scale mass transfer rates for different initial flow rates and as flow rates increase due to increasing aperture. A more detailed look at changes in the aperture distribution during the experiments and simulations is provided by aperture histograms at the beginning of the experiment and at $\langle b \rangle / \langle b_o \rangle$=2.1 (**Figure 6**). The initial histogram shows that the fracture aperture exhibits a slightly skewed distribution with a median ~0.03 mm larger than the mean. Alterations in fracture aperture fields caused by dissolution led to different changes in the aperture distributions for each experiment. For Exp.1, the aperture distribution maintains the same general shape except for the dramatic increase in the largest apertures reflected by the long tail of the distribution (corresponding to the dissolution channels), whereas Exp. 2 exhibits a general stretching of the distribution, with a more significant increase in the median aperture. The simulations predict the basic features of the histograms well including the shift of the median to larger apertures. The most significant discrepancy between the simulations and experiments occurs for Exp. 2 where the simulation underestimates the magnitude of the largest apertures. This is the result of the discrepancies between the rates of aperture growth near the inflow boundary.

Semivariograms calculated along the long axis of the fractures (mean flow direction) for the initial aperture field and the experimentally measured and simulated fields at $\langle b \rangle / \langle b_o \rangle$=2.1 show changes in the correlation structure of the aperture field caused by dissolution (**Figure 7**). The semivariogram for the initial aperture field shows that the field has a correlation length (λ) of about 0.5 mm, where λ is defined as the separation at which the semivariance exceeds (1-1/e)σ_b^2 and σ_b^2 is the variance of the aperture field. The semivariogram of the initial aperture field also reveals mild periodic fluctuations in the initial aperture field with a wavelength of ~2 mm, which are also evident in **Figure 2**.

For Exp. 1, dissolution does not significantly alter the small-scale ($<\lambda$) variability of the aperture field, but the enhanced aperture variability observed in **Plate 1a** is clearly evident at scales greater than λ. By contrast, in Exp. 2 dissolution results in a reduction of small-scale aperture variability for scales to about 1 cm, above which, the fracture-scale trend in aperture causes a monotonic increase in the semivariograms. The simulations for both experiments underestimate the increase in aperture variability at scales larger than λ, which is a result of the small-scale differences in dissolution rates observed in **Plate 1c**. However, the trends in the long-wavelength aperture variability are reproduced well for both experiments supporting the qualitative observation of good agreement of the large-scale features observed in **Plates 1a** and **1b**.

The presence or absence of distinct dissolution channels and the magnitude of the apertures within the channels will significantly influence alterations in fracture transmissivity over time. **Figure 8** shows changes in aperture integrated parallel ($\Delta\overline{b}(y)$) and perpendicular to the flow direction ($\Delta\overline{b}(x)$) for the experiments and the corresponding simulations at $\langle b\rangle/\langle b_o\rangle$=1.3, 1.7 and 2.1. The plots of $\Delta\overline{b}(x)$ demonstrate that for Exp. 1, the aperture growth is much larger near the inflow end of the fracture with very little alteration near the outflow end, whereas the more uniform aperture growth observed in Exp. 2 results in a much flatter $\Delta\overline{b}(x)$ profile, with measurable growth occurring near the outflow at $\langle b\rangle/\langle b_o\rangle$=2.1. The simulations predict the changes in $\Delta\overline{b}(x)$ fairly well, with the most significant discrepancies occurring for Exp. 2 within 20 mm of the inflow where the simulation underestimates the measured $\Delta\overline{b}(x)$ by as much as 0.2 mm. The slower simulated dissolution rate in the entry region leads to a slower increase in c' such that further into the fracture the simulation begins to overestimate $\Delta\overline{b}(x)$. These discrepancies between the simulation and Exp. 2 may result from using the asymptotic value of *Sh* in the entry region, which is about 4 mm long for a parallel plate system with mean aperture of 0.126 mm. However, as both the aperture and flow rate (*Pe*) increase, the length required for development of the asymptotic Sherwood number also increases. Thus, it is likely that the discrepancies observed between the experiment and simulation for Exp. 2 represent and accumulation of errors resulting from the use of

the asymptotic value of *Sh* in the zone near the inflow where the concentration profile across the fracture depth is still developing. Though it is beyond the scope of this investigation, incorporating an expression for $Sh(x)$ in the entry region of the fracture would likely improve agreement between simulations and experiment at high *Pe*. However, in most geologic settings, fractures will likely be much larger than the entry length, and these discrepancies that persist over relatively short length scales are unlikely to cause significant fracture-scale errors. The two different initial flow rates result in significant differences in $\Delta\bar{b}(y)$ (**Figure 8**). Exp. 2 exhibits relatively uniform dissolution across the width of the fracture, whereas the distinct channels seen in **Plate 1** for Exp. 1 result in much more variability in the integrated apertures. The simulation for Exp. 2 predicts the experimental results very well, whereas more discrepancies are evident for Exp. 1. However, though the details of the channel formation differ, the overall magnitude and spatial locations of the simulated channels are similar to the experiments.

Flow simulations through the measured and simulated aperture fields provide measures of the influence of changes in fracture aperture on overall fracture transmissivity ($T=b^3g/12\nu$). As discussed in Section 2, the depth-averaged flow equation may overestimate flow through rough-walled fractures, yet it provides a reasonable estimate of the relative change in *T* as the aperture field evolves. **Figure 9** shows *T* estimated from the measured and simulated aperture fields normalized by the initial fracture transmissivity (T_o). As expected from the width-integrated aperture profiles, T/T_o increases more rapidly for Exp. 2 where dissolution occurs more uniformly throughout the fracture. However, despite the slow initial increase in T/T_o for Exp.1, after breakthrough of the dominant channel it is likely that T/T_o will increase dramatically. The simulations predict changes in T/T_o well at early time for both experiments. However, for Exp. 1, the simulations underestimate changes in T/T_o at later times. This reflects the fact that in the simulations, the main dissolution channel reached the outflow end of the fracture slightly slower than in the experiment (**Plate 1a**). Thus, the experiment is exhibiting early signs of channel breakthrough prior to $\langle b\rangle/\langle b_o\rangle$=2.1, whereas the simulation has not quite reached breakthrough. For Exp. 2, the simulation overestimates T/T_o at later times due to the previously discussed discrepancies near the inflow end of

the fracture. Because the dissolution is relatively uniform for Exp. 2, flow through the fracture can be approximated as a one-dimensional process, such that the local regions of small T near the outflow end of the fracture control the overall fracture transmissivity. Despite discrepancies between the experiments and simulations, the model provides estimates of changes in T/T_o that are a significant improvement over those given by the cubic law applied at the fracture scale.

Our simulations thus far have used the full resolution of the measured data, requiring fairly large computational grids (1160 x 1816 grid blocks) to simulate dissolution in the 9.9 x 15.2 cm fracture. To use this model to investigate scaling properties of fracture dissolution will require coarser grids, which may alter the growth of dissolution channels. To evaluate the influence of grid resolution on simulations, we created a series of coarse-grid aperture fields. We sequentially reduced resolution by geometrically averaging sets of four adjacent grid blocks to yield initial aperture fields with grid resolutions of $2\Delta x$, $4\Delta x$, $8\Delta x$, and $16\Delta x$. Thus, the coarsest resolution ($16\Delta x$ = 1.3 mm) is almost 3 times the correlation length of the initial aperture field (~0.5 mm), resulting in significant loss of small-scale variability in the flow field. Dissolution simulations in each of these fields using the same initial and boundary conditions used for the full field simulations shows the influence of grid resolution on the formation and growth of dissolution channels. **Figure 10** shows apertures integrated across the fracture width and in the flow direction for a subset (Δx, $4\Delta x$, and $16\Delta x$) of these simulations at $\langle b \rangle / \langle b_o \rangle$=1.3, 1.7 and 2.1. The results demonstrate that significant discrepancies between predicted dissolution patterns are not observed until a resolution of $16\Delta x$ at which point the location of the channels for simulation 1 are noticeably different, yet the width-integrated apertures are surprisingly similar for all resolutions. These simulations resulted in negligible deviations of the evolving transmissivities across all grid resolutions.

5.0 Concluding remarks

We have presented a detailed evaluation of an enhanced depth-averaged computational model of fracture dissolution caused by reactive fluid flow. Comparison of simulations to quantitative experimental results in replicated analog fractures subjected to different initial flow rates has provided a comprehensive evaluation of the computational model over a portion of *Pe-Da* parameter space. Small-scale discrepancies between the simulations and experiments result in more spatially uniform dissolution at the scale of λ for the simulations, which leads to simulated Δb fields that exhibit less small-scale variability than was observed for the experiments. Despite these small-scale discrepancies, the large-scale dissolution patterns were predicted quite well by the simulations suggesting that depth-averaged approximations to the three-dimensional governing equations can be used to effectively predict alterations in the fracture aperture caused by dissolution, including the formation of distinct dissolution channels at large Da, and more uniform dissolution with a reduction in small-wavelength aperture variability at low Da. Some additional discrepancies between the simulations and experiments result from the use of the asymptotic value of *Sh* in the entry region of the fracture, which leads to an underestimation of simulated dissolution rates in the region where $x<\sim 0.1 Pe\langle b\rangle$. This region is typically quite small (O(mm)), but for high *Pe* in the relatively short (152 mm) experimental fracture, this resulted in noticeable discrepancies in the inflow region of the fracture. In longer fractures, and/or fractures with slower surface-reaction kinetics these high *Pe* discrepancies will be less significant.

Comparison of our results to fully three-dimensional simulations of dissolution calculated in the same initial aperture fields [*Szymczak and Ladd*, 2004] demonstrates that our depth-averaged model produces remarkably similar results, yet the computational costs of the depth-averaged model are orders of magnitude less than those of the three-dimensional LB-based approach. This allows full-field simulations without the need to subdivide the domain and/or coarsen the grid to solve problems of the scale presented here on single processors. In relatively smooth aperture fields (small $\sigma_b/\langle b\rangle$) the details of

local aperture variability may not be important to the long-term evolution of dissolution channels once the initial channels have formed, which supports the use of sequential grid coarsening as channels evolve [*Szymczak and Ladd*, 2004]. However, for the case of highly heterogeneous aperture fields (large $\sigma_b/\langle b \rangle$) aperture variability in the vicinity of the tip of evolving channels plays a critical role in determining channel evolution [*Cheung and Rajaram*, 2002]. Thus, the ability to fully resolve aperture variability across the entire domain makes the depth-averaged approach presented here an ideal tool for evaluating the influence of parameters such as $\sigma_b/\langle b \rangle$, *Pe* and *Da* on the evolution of dissolution channels and the resulting influence on transport properties over a wide range of scales.

The experimental study used to evaluate the depth-averaged model involved an idealized monomineralic system with the fracture surfaces fixed in space [*Detwiler, et al.*, 2003]. Though this provides an ideal test for the influence of aperture variability and flow rate (*Pe* and *Da*) on dissolutional growth of fractures, other factors may influence or even dominate the growth process under different conditions. Issues such as mineral heterogeneity in the rock surfaces [*Gouze, et al.*, 2003] and the resulting multicomponent chemical reactions and complex evolution of the reactive surface area, stresses acting on the fractures as will be encountered at depth [*Polak, et al.*, 2003], and coupled heat transport in hydrothermal systems [*Andre and Rajaram*, 2005] all add complexity to the fundamental processes that result in alteration of fracture apertures and transmissivity over time. However, our evaluation of the depth-averaged approach through comparison to well controlled, systematic experiments supports this modeling approach as a foundation for developing models that explicitly couple other mechanisms to the dissolution process.

Appendix: Justification for the effective reaction rate (k_{eff}) in Equation (9)

To justify the effective reaction rate expression in (9), we first note that the mass transfer problem for flow between parallel-plates and linear surface reaction on both walls can be formulated as:

$$\frac{3}{2}U(1-\frac{4z^2}{b^2})\frac{\partial c}{\partial x}-D_m\frac{\partial^2 c}{\partial z^2}=0,-\frac{b}{2}\le z\le\frac{b}{2} \qquad \text{(A.1)}$$

where U is the mean fluid and z is the coordinate perpendicular to the flow direction (across the aperture), with boundary conditions:

$$-D_m\frac{\partial c}{\partial z}=k(c_s-c) \text{ on } z=\pm\frac{b}{2} \qquad \text{(A.2)}$$

In classical mass transfer theory for ducts, the in-plane diffusion terms are typically neglected, as in (A.1). In the mass transfer theory for ducts, the effective reaction rate k_{eff} is defined so that the mixing-cup concentration or flux-averaged concentration (c_m) at any cross-section satisfies:

$$q\frac{dc_m}{dx}=k_{eff}(c_s-c_m) \qquad \text{(A.3)}$$

For an extremely rapid surface reaction rate, the surface reaction may be approximated as completed everywhere along the surfaces at all times, so that the boundary condition (A.2) is replaced with $c=c_s$. This version of the problem is most commonly treated in textbooks on heat and mass transfer, and the corresponding expression for the asymptotic (i.e. beyond the entry length) k_{eff} is given by (7). The more general problem defined in (A.1) and (A.2) has been treated in the mass transfer literature, although not widely discussed in textbooks. To quantify k_{eff}, (A.1) and (A.2) are formally solved by separation of variables, leading to a series solution in terms of eigenfunctions with corresponding eigenvalues. Subsequently, the asymptotic k_{eff} is related to the smallest

eigenvalue that decays at the slowest rate. *Walker and Davies* [1974] showed that the eigenfunctions for this problem are confluent hypergeometric functions and presented power-series approximations for the smallest eigenvalue, which is related to the asymptotic Sherwood number. In **Figure A.1** we present a comparison between (11), the Walker-Davies solution and k_{eff} estimated from numerical simulation of (A.1). We also show a comparison between the modified version of (11) and a corresponding numerical simulation for the case of a single reacting wall.

Acknowledgments

This work was performed under the auspices of the U.S. Department of Energy by University of California, Lawrence Livermore National Laboratory under Contract W-7405-Eng-48 and University of Colorado under Contract DE-FG03-96ER14590. Funding was provided by the U.S. Department of Energy's Office of Basic Energy Sciences, Geosciences Program and the Lawrence Livermore National Laboratory Science and Technology Office.

Table 1: Summary of experimental conditions

Experiment	$\langle b_o \rangle$ (cm)	σ_o (cm)	λ (cm)	Q_o (cm^3/s)	Pe_o	Da_o (1)
1	0.0126	0.0049	0.05	0.0036	54	2.7
2				0.0145	216	0.67

(1) Calculated using the $k(0.05) = 6.4 \cdot 10^{-5}$ cm/s calculated using (11).

Table 2: Summary of simulation parameters

Parameter	Value	Source
D_m (1)	$6.77 \cdot 10^{-6}$ cm^2/s	[*Mullin and Amatavivadhana*, 1967]
ρ_f (1)	1.19 g/cm^3	
ρ_r	2.238 g/cm^3	
c_s (1)	25.6 % by weight	
c_o	0.95 c_s	[*Detwiler, et al.*, 2003]
A	$8.4 \cdot 10^{-5}$ cm/s	[*Koziejowska and Sangwal*, 1988]
B	0.039	
A′	$1.244 \cdot 10^{-4}$ cm/s	Calculated for this study to approximate data of *Koziejowska and Sangwal* [1988] using (11); see **Figure 3**.
B′	0.033	
Sh	2.43	[*Kays*, 1966]
Δx	0.0083 cm	[*Detwiler, et al.*, 2003]
$\Delta h_{exp\ 1}$	0.9 cm	Adjusted to match measured flow rates
$\Delta h_{exp\ 2}$	3.6 cm	

(1) These values are presented for 27.5° C, the temperature measured at the inflow of the experiments presented by Detwiler et al. [2003].

Figure Captions

Plate 1: Experimentally measured and simulated Δb fields in the 9.9 x 15.2 cm fracture for Exp. 1 (a) and Exp. 2 (b) corresponding to times at which $\langle b \rangle / \langle b_o \rangle$=1.3, 1.7 and 2.1. At high Da (Exp. 1) the early formation of distinct channels leads to the eventual breakthrough of a single dominant channel, whereas at low Da (Exp. 2) dissolution is more uniform throughout the fracture with minimal channel formation. Frame (c) shows the initial aperture field (top) and Δb fields for the Exp. 1 experiment (middle) and simulation (bottom) for the highlighted region in (a). Despite discrepancies in the small-scale details, the simulations predict the large-scale features of both experiments quite well.

Figure 1: Dissolution rates ($\Delta b/\Delta t$) plotted against Da' for fracture apertures ranging from 0 to 1 mm. The solid line represents the dissolution rate predicted by (4) using the expression for k_{eff} given by (9), using a concentration of c_o and KDP reaction kinetics provided in **Table 2**. The dashed lines represent the reaction-limited mass transfer rate (5) and the transport-limited mass transfer rate (7). The model for k_{eff} correctly predicts the expected behavior accurately as $Da' \rightarrow 0$ and as $Da' \rightarrow \infty$ and provides a smooth transition between the two mass transfer regimes near Da'=1.

Figure 2: Initial 9.9 x 15.2 cm aperture field measured at 0.083 x 0.083 cm resolution using light transmission techniques. The grayscale represents the magnitude of the aperture with black = 0 and white ≥ 0.25 mm.

Figure 3: Dissolution rate for a KDP surface plotted against the under-saturation ($1-c'$) of the fluid at the surface. The solid line represents the model proposed by *Koziejowska and Sangwal* [1988] and the data points represent the simplified version of the model (11) used in the current study. The relevant parameter values are provided in **Table 2**.

Figure 4: Cumulative effluent mass plotted against time for the experiments (+) and simulations (lines). The discrepancy between the experiment and simulation for Exp. 1 was due to a slow alteration in the hydraulic gradient caused by precipitation of KDP at the outlet point. Removal of the precipitated KDP at ~4 and 12.5 hours resulted in a corrected flow that was closer to the simulated flow rate.

Figure 5: Normalized change in mean aperture plotted against time for Exp. 1 (*) and Exp. 2 (+) and the corresponding simulations (solid lines). The missing data point at ~10 hours reflects a brief imaging system malfunction during the experiment.

Figure 6: Histograms of the fracture aperture fields for the initial fracture (bold solid line) and Exp. 1 (*) and Exp. 2 (+) at $\langle b \rangle / \langle b_o \rangle$=2.1 and the corresponding simulations (solid lines).

Figure 7: Semivariograms measured in the mean flow direction (long axis of the fracture), normalized by the variance of the initial aperture field, for the initial aperture field (bold solid line) and Exp. 1 (*) and Exp. 2 (+) with the corresponding simulations (solid lines).

Figure 8: Fracture aperture integrated over the length (top) and width (bottom) of the fracture at $\langle b \rangle / \langle b_o \rangle$=1.3, 1.7 and 2.1 for the experiments (solid lines) and simulations (dashed lines).

Figure 9: Normalized transmissivity (T/T_o) for Exp. 1 (*), Exp. 2 (+) and the corresponding simulations (solid lines), and the cubic law (bold solid line).

Figure 10: Simulated fracture apertures at $\langle b \rangle / \langle b_o \rangle$=1.3, 1.7 and 2.1 integrated over the length (top) and width (bottom) of the fracture at $\langle b \rangle / \langle b_o \rangle$= 2.0 for grid resolutions of Δx (solid line), $4\Delta x$ (+) and $16\Delta x$ (o).

Figure A.1: Comparison of nondimensional effective reaction rates calculated by numerical solution of (A.1), the Walker-Davies solution and equation (11) for two dissolving surfaces (a) and a single dissolving surface (b).

6.0 References

Alves, M. A., P. J. Oliveira, and F. T. Pinho, A convergent and universally bounded interpolation scheme for the treatment of advection, *International Journal for Numerical Methods in Fluids*, *41*, 47-75, 2003.

Andre, B. J., and H. Rajaram, Dissolution of limestone fractures by cooling waters: Early development of hypogene karst systems, *Water Resources Research*, *41*, doi:10.1029/2004WR003331, 2005.

Bekri, S., J. F. Thovert, and P. M. Adler, Dissolution and deposition in fractures, *Engineering Geology*, *48*, 283-308, 1997.

Brown, S. R., Simple Mathematical-Model of a Rough Fracture, *Journal of Geophysical Research-Solid Earth*, *100*, 5941-5952, 1995.

Brush, D. J., and N. R. Thomson, Fluid flow in synthetic rough-walled fractures: Navier-Stokes, Stokes, and local cubic law simulations, *Water Resources Research*, *39*, doi:10.1029/2002WR001346, 2003.

Cheung, W., and H. Rajaram, Dissolution finger growth in variable aperture fractures: Role of the tip-region flow field, *Geophysical Research Letters*, *29*, 2002.

Cheung, W. W., Toward a better understanding of fissure growth in karst formations: Investigations from genesis to maturation and the influence of fracture-matrix interactions, Ph.D. thesis, 168 pp, University of Colorado, Boulder, 2002.

Daccord, G., O. Lietard, and R. Lenormand, Chemical dissolution of a porous-medium by a reactive fluid: 2. Convection vs reaction, behavior diagram, *Chemical Engineering Science*, *48*, 179-186, 1993.

Detwiler, R. L., S. E. Pringle, and R. J. Glass, Measurement of fracture aperture fields using transmitted light: An evaluation of measurement errors and their influence on simulations of flow and transport through a single fracture, *Water Resources Research*, *35*, 2605-2617, 1999.

Detwiler, R. L., H. Rajaram, and R. J. Glass, Solute transport in variable-aperture fractures: An investigation of the relative importance of Taylor dispersion and macrodispersion, *Water Resources Research*, *36*, 1611-1625, 2000.

Detwiler, R. L., H. Rajaram, and R. J. Glass, Nonaqueous-phase-liquid dissolution in variable-aperture fractures: Development of a depth-averaged computational model with comparison to a physical experiment, *Water Resources Research*, *37*, 3115-3129, 2001.

Detwiler, R. L., S. Mehl, H. Rajaram, and W. W. Cheung, Comparison of an algebraic multigrid algorithm to two iterative solvers used for modeling ground water flow and transport, *Ground Water*, *40*, 267-272, 2002.

Detwiler, R. L., R. J. Glass, and W. L. Bourcier, Experimental observations of fracture dissolution: The role of Peclet number on evolving aperture variability, *Geophysical Research Letters*, *30*, doi:10.1029/2003GL017396, 2003.

Dijk, P. E., B. Berkowitz, and Y. Yechieli, Measurement and analysis of dissolution patterns in rock fractures, *Water Resources Research*, *38*, doi:10.1029/2001WR000246, 2002.

Durham, W. B., W. L. Bourcier, and E. A. Burton, Direct observation of reactive flow in a single fracture, *Water Resources Research*, *37*, 1-12, 2001.

Golfier, F., C. Zarcone, B. Bazin, R. Lenormand, D. Lasseux, and M. Quintard, On the ability of a Darcy-scale model to capture wormhole formation during the dissolution of a porous medium, *Journal of Fluid Mechanics*, *457*, 213-254, 2002.

Gouze, P., C. Noiriel, C. Bruderer, D. Loggia, and R. Leprovost, X-ray tomography characterization of fracture surfaces during dissolution, *Geophysical Research Letters*, *30*, doi:10.1029/2002GL016755, 2003.

Hanna, R. B., and H. Rajaram, Influence of aperture variability on dissolutional growth of fissures in karst formations, *Water Resources Research*, *34*, 2843-2853, 1998.

Hoefner, M. L., and H. S. Fogler, Pore evolution and channel formation during flow and reaction in porous-media, *Aiche Journal*, *34*, 45-54, 1988.

Johns, L. E., and a. E. Degance, Dispersion approximations to multicomponent convective diffusion equation for chemically active systems, *Chemical Engineering Science*, *30*, 1065-1067, 1975.

Jähne, B., *Practical handbook on image processing for scientific applications*, x, 589 p., [523] p. of plates, CRC, Boca Raton, Fla., 1997.

Kays, W. M., *Convective heat and mass transfer*, xxvi, 387 p., McGraw-Hill, New York, 1966.

Koziejowska, a., and K. Sangwal, Surface micromorphology and dissolution kinetics of potassium dihydrogen phosphate (Kdp) crystals in undersaturated aqueous-solutions, *Journal of Materials Science*, *23*, 2989-2994, 1988.

Mourzenko, V. V., J. F. Thovert, and P. M. Adler, Permeability of a single fracture - validity of the Reynolds-equation, *Journal De Physique Ii*, *5*, 465-482, 1995.

Mullin, J. W., and A. Amatavivadhana, Growth kinetics of ammonium- and potassium-dihydrogen phosphate crystals, *Journal of Applied Chemistry*, *17*, 151-156, 1967.

Nicholl, M. J., H. Rajaram, R. J. Glass, and R. Detwiler, Saturated flow in a single fracture: Evaluation of the Reynolds equation in measured aperture fields, *Water Resources Research*, *35*, 3361-3373, 1999.

O'brien, G. S., C. J. Bean, and F. McDermott, Numerical investigations of passive and reactive flow through generic single fractures with heterogeneous permeability, *Earth and Planetary Science Letters*, *213*, 271-284, 2003.

Polak, A., D. Elsworth, H. Yasuhara, A. S. Grader, and P. M. Halleck, Permeability reduction of a natural fracture under net dissolution by hydrothermal fluids, *Geophysical Research Letters*, *30*, doi:10.1029/2003GL017575, 2003.

Rohsenow, W. M., and H. Y. Choi, *Heat, mass, and momentum transfer*, 537 p., Prentice-Hall, Englewood Cliffs, N.J., 1961.

Ruge, J. W. S., K., Algebraic multigrid, in *Multigrid methods: theory, applications, and supercomputing*, edited by S. F. McCormick, pp. xiv, 644 p., M. Dekker, New York, 1988.

Szymczak, P., and a. J. C. Ladd, Boundary conditions for stochastic solutions of the convection-diffusion equation, *Physical Review E*, *68*, 2003.

Szymczak, P., and a. J. C. Ladd, Microscopic simulations of fracture dissolution, *Geophysical Research Letters*, *31*, doi:10.1029/2004GL021297, 2004.

Verberg, R., and a. J. C. Ladd, Simulation of chemical erosion in rough fractures, *Physical Review E*, *65*, doi:10.1103/PhysRevE.65.056311, 2002.

Walker, G., and T. Davies, Mass-transfer in laminar-flow between parallel permeable plates, *AIChe Journal*, *20*, 881-889, 1974.

Yeo, I. W., M. H. De Freitas, and R. W. Zimmerman, Effect of shear displacement on the aperture and permeability of a rock fracture, *International Journal of Rock Mechanics and Mining Sciences*, *35*, 1051-1070, 1998.

Plate 1

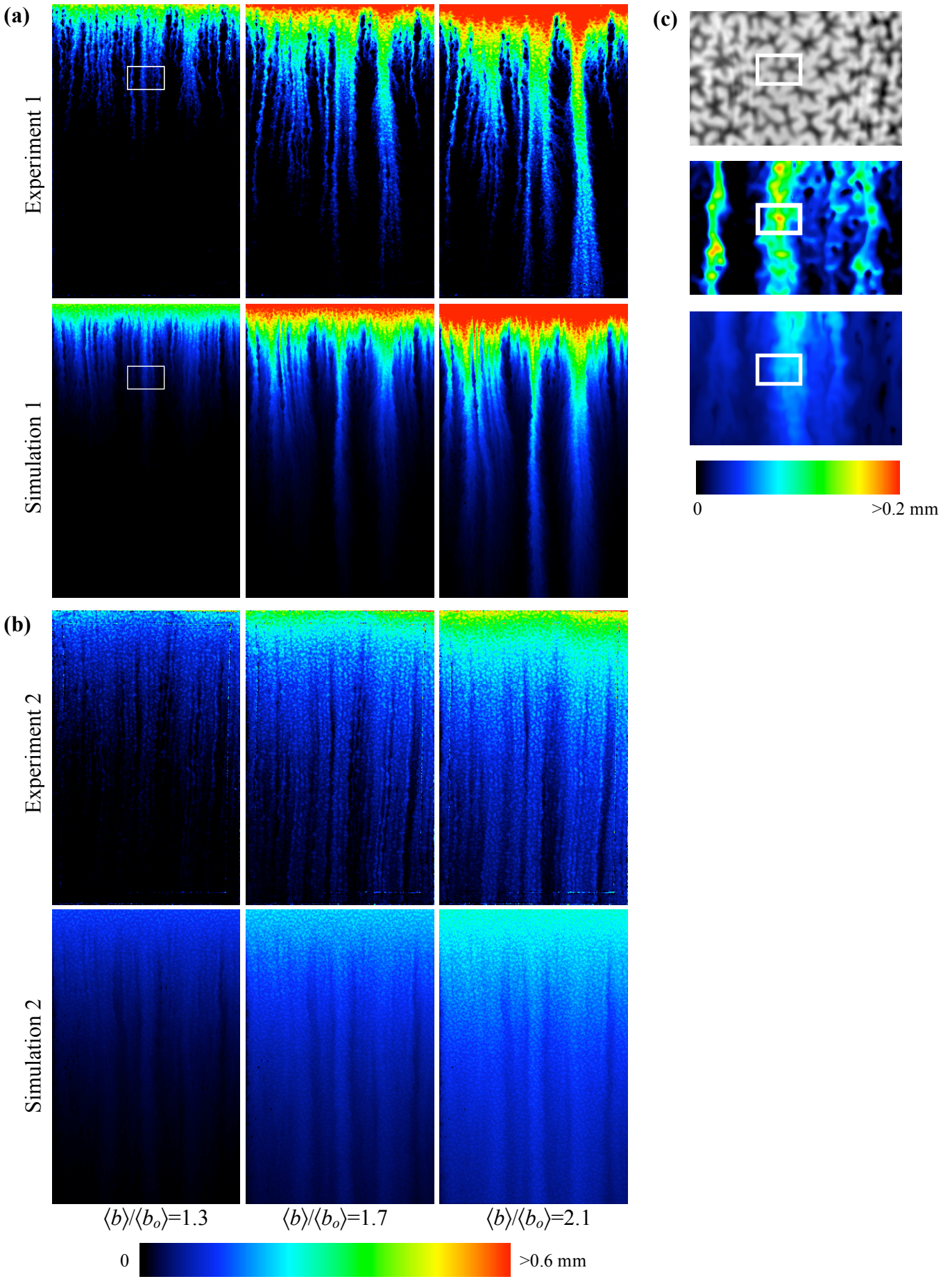
(a)
Experiment 1
Simulation 1
(b)
Experiment 2
Simulation 2
⟨b⟩/⟨b_o⟩=1.3
⟨b⟩/⟨b_o⟩=1.7
⟨b⟩/⟨b_o⟩=2.1
0
>0.6 mm
(c)
0
>0.2 mm

Figure 1

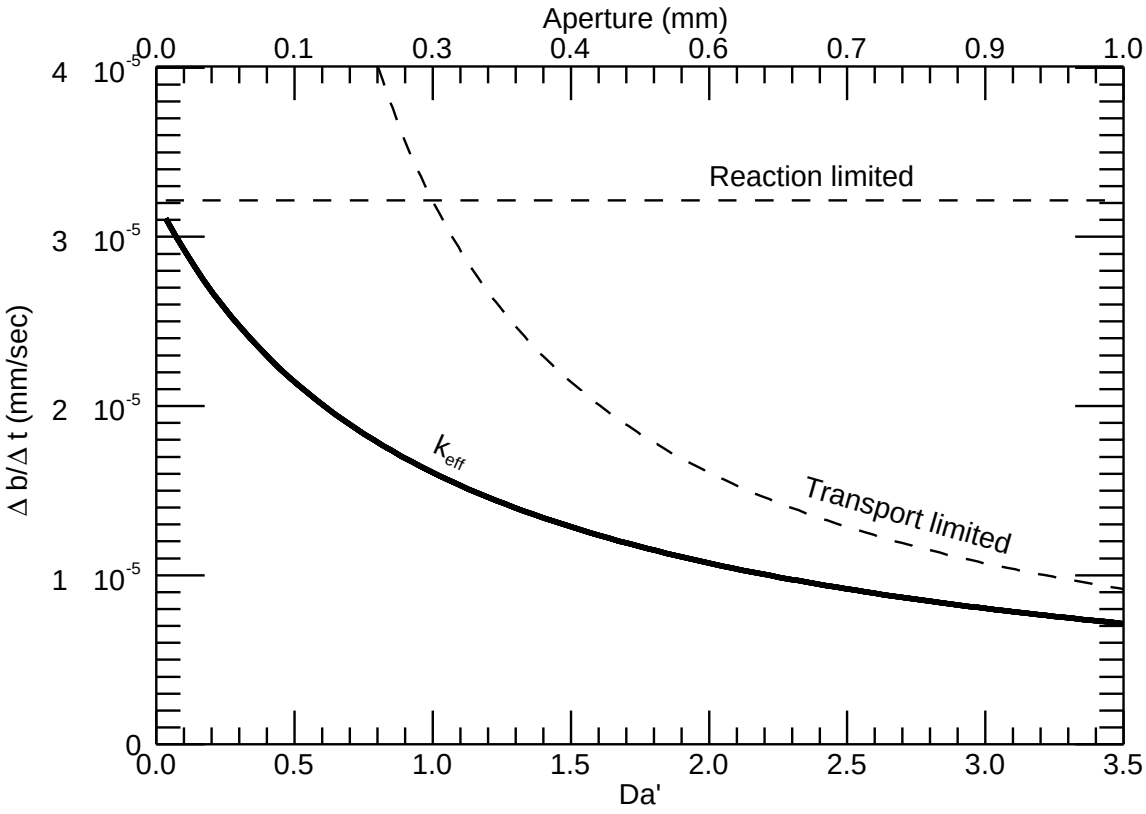

Figure 2

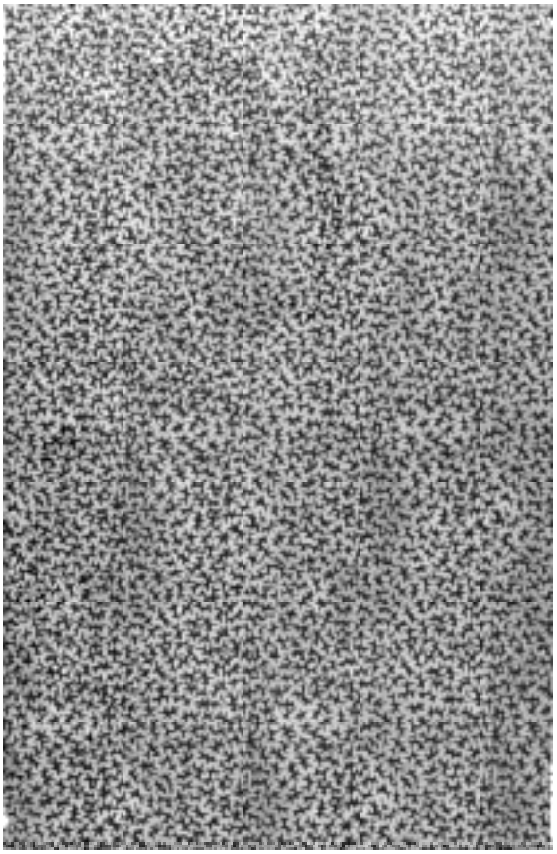

Figure 3

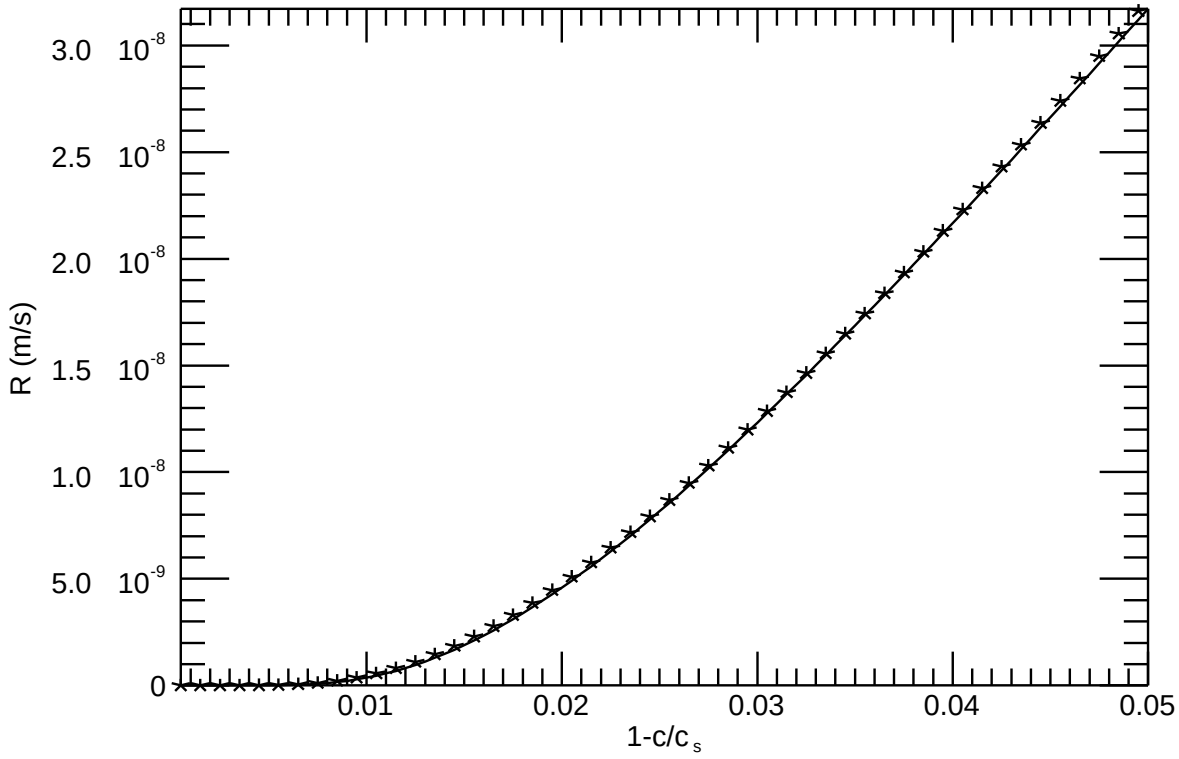

Figure 4

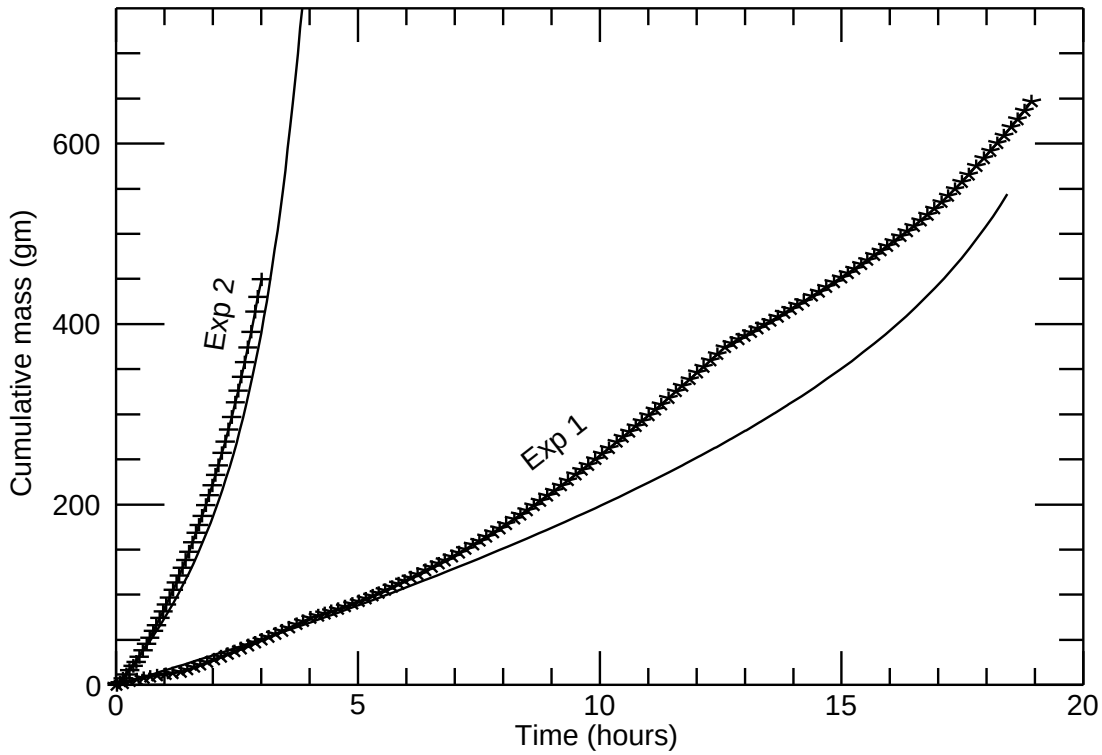

Figure 5

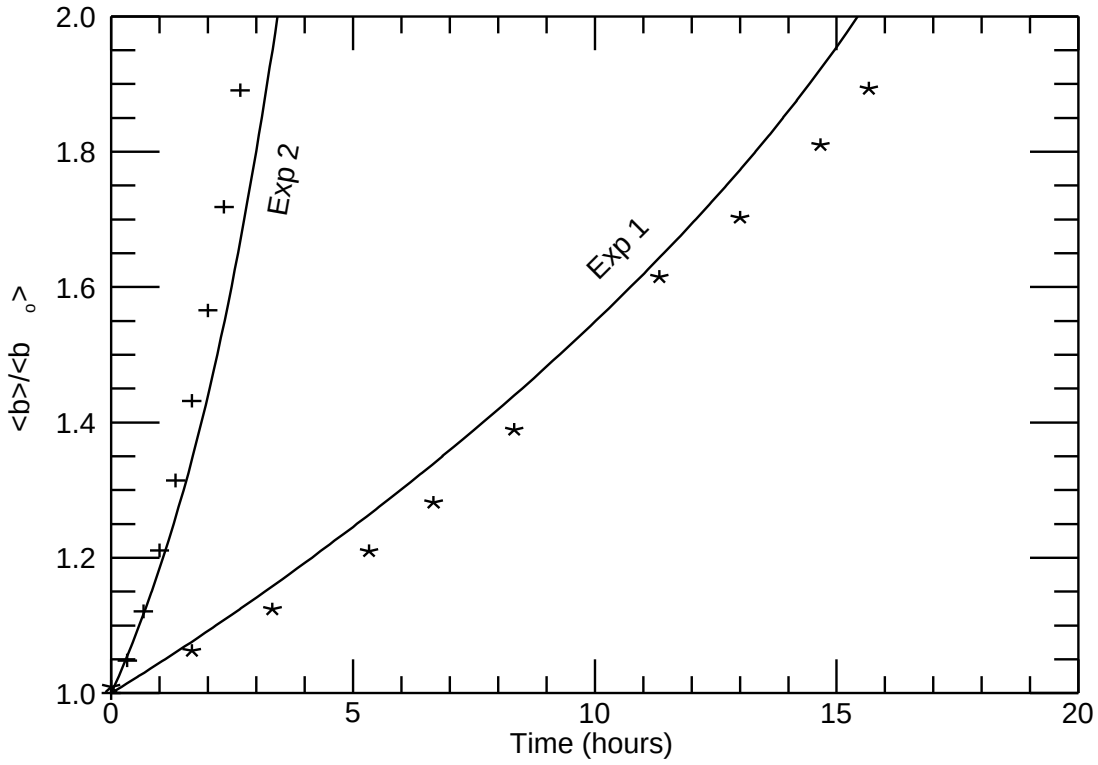

Figure 6

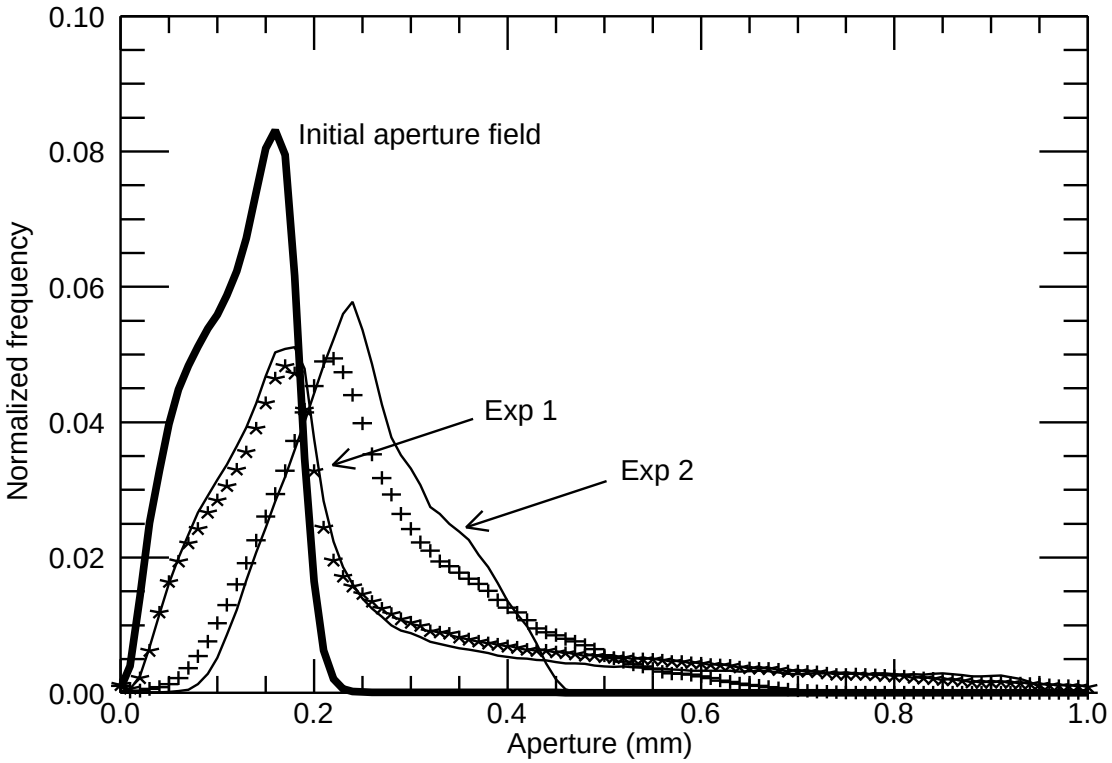

Figure 7

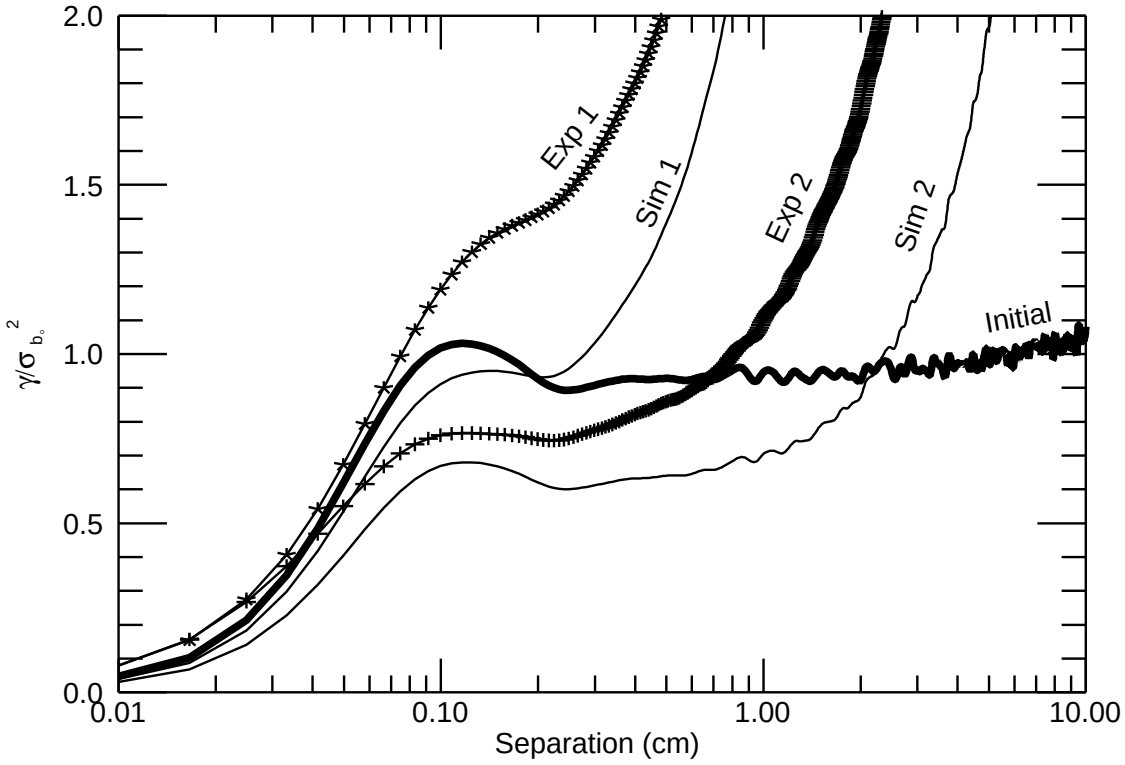

Figure 9

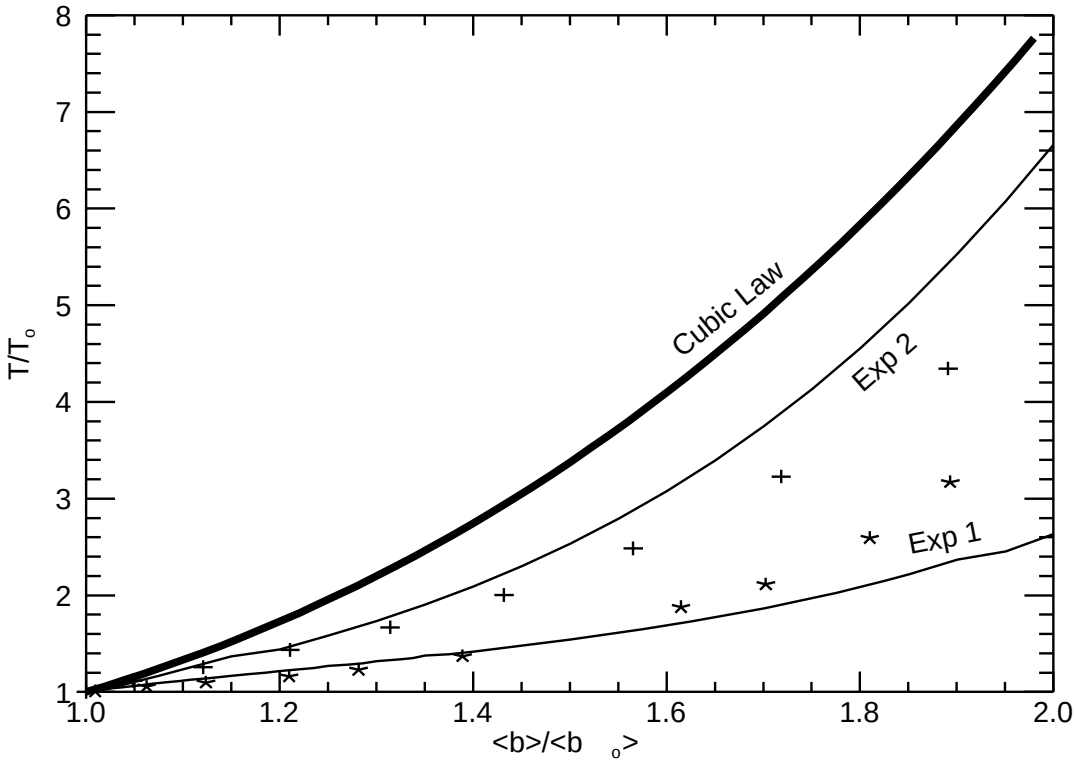

Figure 8

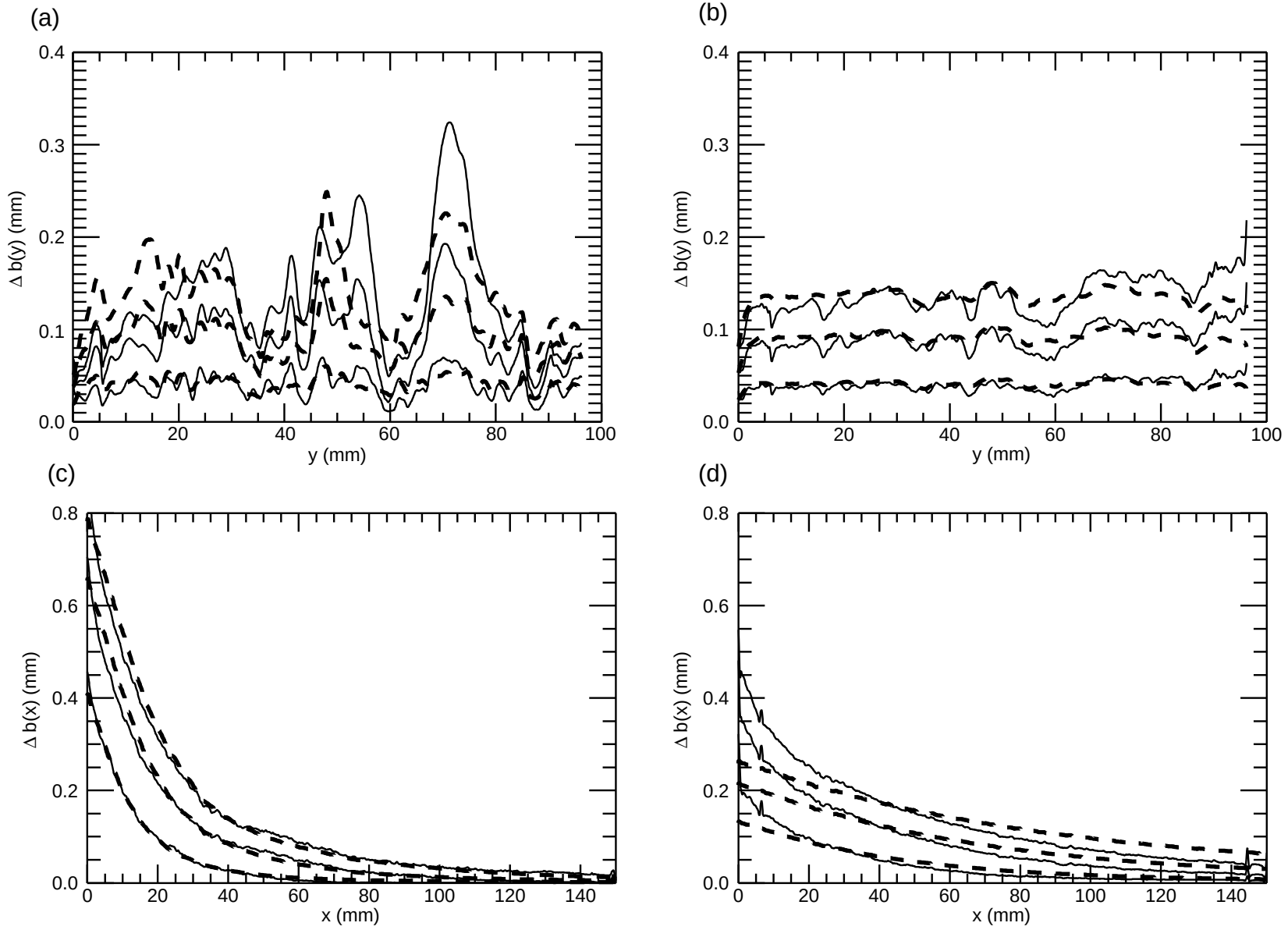
(a)
(b)
(c)
(d)
Δ b(y) (mm)
y (mm)
Δ b(x) (mm)
x (mm)
0.0
0.1
0.2
0.3
0.4
0.6
0.8
0
20
40
60
80
100
120
140

Figure 10

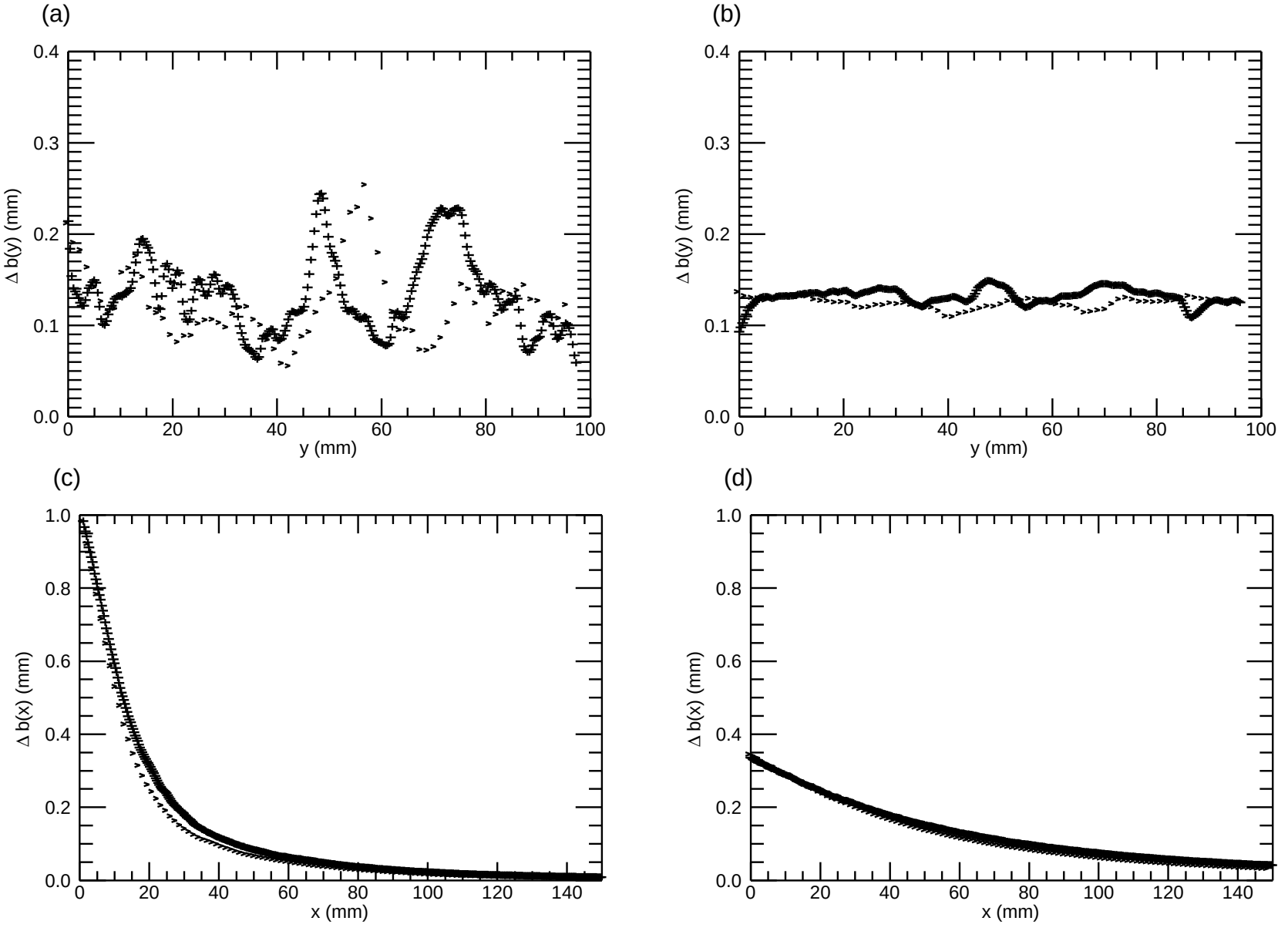
(a)
(b)
(c)
(d)
Δ b(y) (mm)
y (mm)
Δ b(x) (mm)
x (mm)
0.0
0.1
0.2
0.3
0.4
0.6
0.8
1.0
0
20
40
60
80
100
120
140